Pose Control of Millimeter-Scale Objects in a Laser-Powered Thermocapillary Manipulation Platform

Franco Nicolas Piñan Basualdo, Olivier Stéphan, Aude Bolopion, Michaël Gauthier, Pierre Lambert

Pose control of millimeter-scale objects in a laser-powered thermocapillary manipulation platform

Franco N. Piñan Basualdo, Olivier Stephan, A. Bolopion, Michaël Gauthier, Pierre Lambert

***Abstract*—The miniaturization of technological components requires tools capable to manipulate them. Non-contact micromanipulation has recently gained popularity since it minimizes component damage and adhesion problems. However, the simultaneous position and orientation (pose) control using non-contact tools remains an open challenge. In this work, we propose the pose control of millimeter-scale structures at the air-water interface using laser-powered thermocapillary flows. We achieve autonomous pose control by steering two laser spots around the structure in a closed-loop manner. The controller consists of a linear pose controller and a model inversion. The pose controller defines the required force and torque to reach the target. The model inversion defines the required laser positions to obtain said force and torque. This inversion is performed with an optimization algorithm, without any prescribed strategy. The pose stabilization was validated experimentally, obtaining a position and orientation precision of 0.15 body lengths and 2°, respectively. Additionally, we show the experimental path-following with independent orientation control, obtaining a similar position precision.**

***Index Terms*—Automation at Micro Scales – Micro Robots – Motion Control – Non-contact actuation**

I. Introduction

MINIATURIZATION of technological components requires the development of novel manipulation and assembly techniques. Indeed, the handling of small components (typically below $1\,\mathrm{mm}$) needs to account for adhesion forces dominating over inertia [1]. In the literature, one can find several proposals to achieve robotic manipulation of microscale objects [2]. In particular, the simultaneous and independent position and orientation control is often called pose control.

One option to control micrometer-sized objects is non-contact manipulation [3], this is, by externally controlling a potential field to drive objects. Indeed, at the microscale, non-contact manipulation presents several advantages [4]. First, the absence of contact between the manipulator and the manipulated objects prevents the adhesion between them. Second, since the exerted forces are limited, there is little risk of component damage. Among the different non-contact manipulation techniques, we found magnetic, acoustic, optical, and electrical manipulation among the most common ones. Each technique presents different advantages and disadvantages, which are discussed below.

Manipulation of magnetic particles can be achieved by externally controlling the magnetic field. Indeed, magnetic field gradients can be used to displace magnetic objects [5]–[7], and magnetic torques can be used, for example, to actuate helical swimmers [8], [9]. By combining both previous effects, it is possible to achieve pose control of a single object [10], [11]. Moreover, some techniques have been developed for the independent position control of multiple particles [5], [12], [13] (which requires complex magnetic setups), and swarms of magnetic particles [14], [15].

Acoustic manipulation consists in creating and controlling a standing pressure wave to drive the particles [16]–[18]. In this case, the actuation is spatially selective, which allows the simultaneous position control of multiple particles [19]. Although there are proposals to acoustically control the orientation of objects [20], there is no work showing pose control.

Optical manipulation is based on light-matter interactions for actuation. The most well-known example is optical tweezers, which use focused laser beams to create optical traps [21], [22]. Moreover, the use of multiple optical traps allows the pose control of microrobots [23] and the development of optical micro-hands [24]. In this case, the actuation is highly selective, only affecting a small area around the optical trap. Moreover, due to the stable nature of the optical traps, no convoluted algorithms are required to achieve high precision control. The main limitation of this technique is that it depends on the material properties of the optical handles [23] and that optical forces are normally small (around a few pN), limiting their use to the smaller scales.

Finally, electrical manipulation systems can be based on electrophoresis [25] or dielectrophoresis [26]. Electrophoresis is the migration of electrokinetic nanoparticles in the presence of a uniform electric field [27]. Electrophoresis has been proposed as a promising strategy to manipulate nanowires [28] and to control oil microdroplets [29]. Dielectrophoresis is the migration of dielectric particles in the presence of a non-homogeneous time-varying electric field [30]. Dielectrophoresis has been used to manipulate cells [31], [32] and particles [33], [34] inside microfluidic chips. Moreover, dielectrophoretic forces can also be used to rotate non-spherical

Franco N. Piñan Basualdo and Pierre Lambert are with the Transfers Interfaces and Processes (TIPs) department, Université Libre de Bruxelles, Av. Franklin Roosevelt 50, 1050 Brussels, Belgium.

Franco N. Piñan Basualdo, Aude Bolopion, and Michaël Gauthier are with the FEMTO-ST Institute, CNRS, Université Bourgogne Franche-Comté, 24 rue Savary, F-25000 Besançon, France.

Olivier Stephan is with the Université Grenoble Alpes, CNRS, LIPhy, F-38000 Grenoble, France.

franco.pinan.basualdo@ulb.be

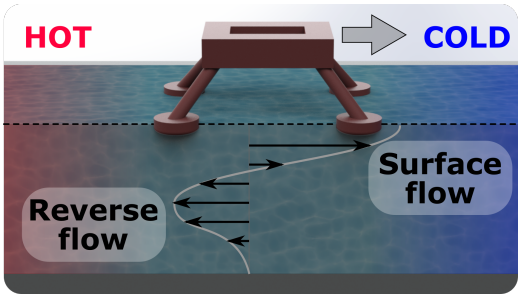

Fig. 1. Schema of the thermocapillary actuation physical principle. A temperature gradient along a fluid interface gives place to an interfacial flow from hot to cold areas [37]. In this work, we profit from this interfacial flow to actuate structures floating on the interface.

objects [35], opening the way toward pose control. Nevertheless, in both cases, the resulting forces are small, limiting their use to the manipulation of micro or nanoparticles.

In conclusion, there is still a lack of an actuation technique that enables both selective manipulation and pose control at the millimeter scale. In that context, we have previously proposed to use laser-powered thermocapillary flows for micromanipulation at the air-water interface [36]. In that work, we showed the feasibility of object manipulation at the interface and the guidance of capillary self-assembly by displacing the laser spot on the interface. Although in that work we showed the control of an object position and orientation, the proposed strategy cannot be considered as pose control, since the object position and orientation were not controlled independently.

In this work, we expand on the mentioned results and propose an alternative to decouple the position and orientation control of the object. The proposal is to use two laser spots and a numerical optimization algorithm to find adequate spot positions to obtain the desired response (translation and rotation velocities). Then, by combining this optimization algorithm with a traditional single input, single output (SISO) PI controllers for each degree of freedom (two for the position and one for the orientation), we achieve true 2D pose control based on non-contact manipulation. Moreover, given the local nature of the thermocapillary flow, these results can be extended to the parallel control of multiple objects, opening the way toward more complex operations at the air-water interface.

The remainder of this work is organized as follows: Section II presents the actuation system and the considered physical models, Section III presents the developed pose control algorithm, Section IV shows the experimental validation of the developed algorithm, and Section V concludes and provides directions for future work.

II. Actuation

A. Physical principle

The proposed actuation principle is based on the generation of a thermocapillary flow. A thermocapillary flow is a flow arising along a fluid interface in the presence of a temperature gradient [37]. The origin of this phenomenon is the temperature dependence of the surface tension. Indeed, in most cases, the surface tension of an interface decreases with a

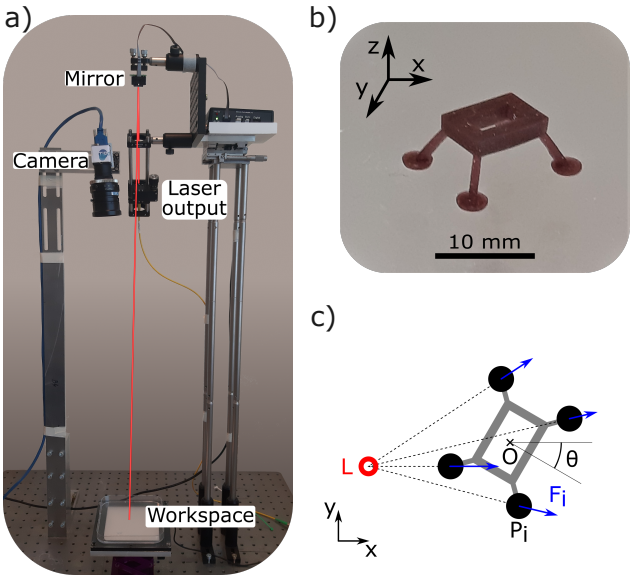

Fig. 2. Pictures of the experimental actuation setup **a**) and actuated structure **b**). The structure actuation schema **c**) shows the forces $\mathbf{F}_i$ applied to the structure feet $\mathbf{P}_i$ by the laser spot $\mathbf{L}$, as well as the structure center $\mathbf{O}$ and orientation θ.

temperature increase. Therefore, warmer areas have a lower interfacial energy excess and tend to expand over cold areas, giving rise to an interfacial flow, as shown in Fig. 1.

One way to generate a local thermocapillary flow is to use an infrared laser to locally heat the surface of a fluid, as shown in Fig. 2a. This local heating causes a local temperature increase, which gives place to a thermocapillary flow around the laser spot due to the Marangoni effect [38]. The resulting flow is divergent from the laser spot at the interface, thus pushing floating objects away from the spot. Then, we can actuate floating objects by displacing the laser spot on the interface.

The effect of the thermocapillary flow is to convey them through drag forces. Therefore, the flow effect is highly dependent on the object's geometry. For the simple case of a small spherical particle at point $\mathbf{P}$, the drag force can be modeled as

$$\mathbf{F} = m\,\ddot{\mathbf{P}} = C_d\left(\mathbf{U} - \dot{\mathbf{P}}\right) \tag{1}$$

where C_d is the viscous drag coefficient, m is the mass of the particle, $\mathbf{U}$ is the thermocapillary flow velocity at the point $\mathbf{P}$, $\dot{\mathbf{P}}$ and $\ddot{\mathbf{P}}$ are the particle velocity and acceleration, respectively. As it has been shown in a previous work [38], the laser-powered thermocapillary flow surface velocity magnitude is inversely proportional to the distance to the laser spot and the flow direction is always away from the laser spot. Thus,

$$\mathbf{U} = \alpha\frac{\mathbf{P} - \mathbf{L}}{\|\mathbf{P} - \mathbf{L}\|^2} \tag{2}$$

where $\mathbf{L}$ is the laser spot position and α is a constant that depends on the experimental conditions (fluid, particle, and laser properties). Finally, by replacing (2) in (1), we obtain

$$\mathbf{F} = m\,\ddot{\mathbf{P}} = C_d\left(\alpha\frac{\mathbf{P} - \mathbf{L}}{\|\mathbf{P} - \mathbf{L}\|^2} - \dot{\mathbf{P}}\right) \tag{3}$$

which expresses the force exerted by the flow on the particle as a function of its position relative to the laser spot and its velocity.

B. Multiple-legged structure actuation model

In this section, we consider the case of multiple-legged structures that stand on the interface on a set of N_p feet as the example shown in Fig. 2b. To model the response of the structure to the thermocapillary actuation, we consider the forces $\mathbf{F}_i$ exerted by the flow on each foot $\mathbf{P}_i$, as shown in Fig. 2c for the case of a four-legged structure. As a first approximation, these forces can be modeled using (3) by replacing $\mathbf{P}$ by $\mathbf{P}_i$. On the other hand, since the structure behaves like a rigid solid, the position of each foot is a function of its geometric center $\mathbf{O} = \sum \mathbf{P}_i / N_P$ and its orientation θ. Indeed, the velocity of each foot can be written as

$$\dot{\mathbf{P}}_i = \dot{\mathbf{O}} + \boldsymbol{\omega} \times (\mathbf{P}_i - \mathbf{O}) \tag{4}$$

where $\boldsymbol{\omega} = \dot{\theta}\,\hat{\mathbf{n}}$ is the rotation vector (direction normal to the interface $\hat{\mathbf{n}}$). Replacing (4) in (3) we obtain

$$\mathbf{F}_i = C_d \left(\alpha \frac{\mathbf{P}_i - \mathbf{L}}{\|\mathbf{P}_i - \mathbf{L}\|^2} - \dot{\mathbf{O}} - \boldsymbol{\omega} \times (\mathbf{P}_i - \mathbf{O}) \right) \tag{5}$$

We can then compute the total force and torque exerted on the structure by adding the effect of the flow on all feet as

$$\begin{cases} m\ddot{\mathbf{O}} = \sum \mathbf{F}_i \\ I\ddot{\theta} = \sum (\mathbf{P}_i - \mathbf{O}) \times \mathbf{F}_i \end{cases} \tag{6}$$

where m and I are the structure mass and moment of inertia, respectively. By replacing (5) in (6) and simplifying the expressions we find

$$\begin{cases} \tau_t\, \ddot{\mathbf{O}} + \dot{\mathbf{O}} = \dfrac{\alpha}{N_P} \sum \dfrac{\mathbf{P}_i - \mathbf{L}}{\|\mathbf{P}_i - \mathbf{L}\|^2}. \\ \tau_r\, \ddot{\theta} + \dot{\theta} = \dfrac{\alpha\,(\mathbf{L} - \mathbf{O}) \times \left(\sum \frac{\mathbf{P}_i - \mathbf{L}}{\|\mathbf{P}_i - \mathbf{L}\|^2} \right)}{\sum \|\mathbf{P}_i - \mathbf{O}\|^2} \end{cases} \tag{7}$$

where $\tau_t = m/\left(C_d\, N_p\right)$ and $\tau_r = I/\left(C_d \sum \|\mathbf{P}_i - \mathbf{O}\|^2\right)$ represent the characteristic time of the translation and rotation dynamic systems, respectively.

In the presence of several laser spots $\mathbf{L}_j$, we can approximate the total effect as the addition of the effect of each spot, as long as they are sufficiently apart from each other. In that case, we can extend (7) to multiple laser spots as:

$$\begin{cases} \tau_t\, \ddot{\mathbf{O}} + \dot{\mathbf{O}} = \dfrac{\alpha}{N_P} \sum\limits_{i,j} \dfrac{\mathbf{P}_i - \mathbf{L}_j}{\|\mathbf{P}_i - \mathbf{L}_j\|^2} \\ \tau_r\, \ddot{\theta} + \dot{\theta} = \dfrac{\alpha \sum\limits_{i,j} \left((\mathbf{L}_j - \mathbf{O}) \times \left(\frac{\mathbf{P}_i - \mathbf{L}_j}{\|\mathbf{P}_i - \mathbf{L}_j\|^2} \right) \right)}{\sum\limits_{i} \|\mathbf{P}_i - \mathbf{O}\|^2}. \end{cases} \tag{8}$$

The model (8) allows us to estimate the structure response to given laser spot positions. However, for the pose control purpose, the challenge is to find the laser spot positions that would lead to the desired structure response, this is, to invert the model. As it can be seen, the direct model (8), with the laser spots position as the input and the structure pose as the output, is non-linear and cannot be analytically inverted. The proposed solution is, thus, to invert the model numerically, as explained in the following section.

III. Control strategies

To control the system (8), we first propose a change of variables. We define the variables $\mathbf{C}$ and Ω as:

$$\begin{cases} \mathbf{C} = \dfrac{\alpha}{N_P} \sum\limits_{i,j} \dfrac{\mathbf{P}_i - \mathbf{L}_j}{\|\mathbf{P}_i - \mathbf{L}_j\|^2} \\ \Omega = \dfrac{\alpha \sum\limits_{i,j} \left((\mathbf{L}_j - \mathbf{O}) \times \left(\frac{\mathbf{P}_i - \mathbf{L}_j}{\|\mathbf{P}_i - \mathbf{L}_j\|^2} \right) \right)}{\sum\limits_{i} \|\mathbf{P}_i - \mathbf{O}\|^2} \end{cases} \tag{9}$$

Then, the composition of this change of variables and the system (8), with $\mathbf{C}$ and Ω as the input, and $\mathbf{O}$ and θ as the output results:

$$\begin{cases} \tau_t\, \ddot{\mathbf{O}} + \dot{\mathbf{O}} = \mathbf{C} \\ \tau_r\, \ddot{\theta} + \dot{\theta} = \Omega. \end{cases} \tag{10}$$

With this definition, the system (10) is trivial to control since translation and rotation are decoupled. The complexity is now to find the laser spots positions $\mathbf{L}_j$ that would generate such values of $\mathbf{C}$ and Ω by solving (9). Since (9) has three independent outputs (C_x, C_y and Ω), we choose to use two laser spots to have four independent inputs (L_{1_x}, L_{1_y}, L_{2_x} and L_{2_y}) to solve it. We propose, then, to use a numerical model inversion to find the required spot positions.

A. Numerical model inversion

The objective of the numerical model inversion is to find the laser positions $\mathbf{X} = (L_{1_x}, L_{1_y}, L_{2_x}, L_{2_y})$ that would generate the desired values $\mathbf{Y}_d = (C_x, C_y, \Omega)_d$. This non-linear system can be solved through numerical optimization, as it has been done to find the coil's currents in magnetic manipulation systems [5], [39]. If we now define the vector function f as the non-linear model (9), so that $\mathbf{Y} = f(\mathbf{X})$, we can approach the solution by minimizing $\|\mathbf{Y}_d - f(\mathbf{X})\|$, that is, solving a linear least squares problem. Among the different alternatives for numerical minimization, we decided to use the Levenberg–Marquardt algorithm [40], [41], and in particular, the MATLAB implementation [42].

The Levenberg–Marquardt algorithm interpolates between the Gauss-Newton and gradient descent methods. Briefly, the algorithm receives the non-linear system f, the objective $\mathbf{Y}_d$, and an initial guess $\mathbf{X}_0$. Then, it computes the error $\mathbf{E} = f(\mathbf{X}_0) - \mathbf{Y}_d$, and estimates numerically the Jacobian of f at $\mathbf{X}_0$ ($\mathrm{J}(\mathbf{X}_0)$). Based on these estimations, it proposes a new guess $\mathbf{X} = \mathbf{X}_0 + \delta$ where δ is the solution to $\left(\mathrm{J}^T \times \mathrm{J} + \lambda\, I\right)\delta = \mathrm{J}^T\mathbf{E}$. The parameter λ is adjusted according to the evolution of the minimization. If the new proposal reduces the error, $\mathbf{X}_0$ is updated and λ is reduced. If not, λ is increased, and a new guess is made. Finally, by repeating the process, $\mathbf{X}_0$ iteratively approaches a solution to the problem. In our case, since there are 4 input variables and 3 output variables, if the system can be solved, there is normally more than one solution. Therefore, the found solution

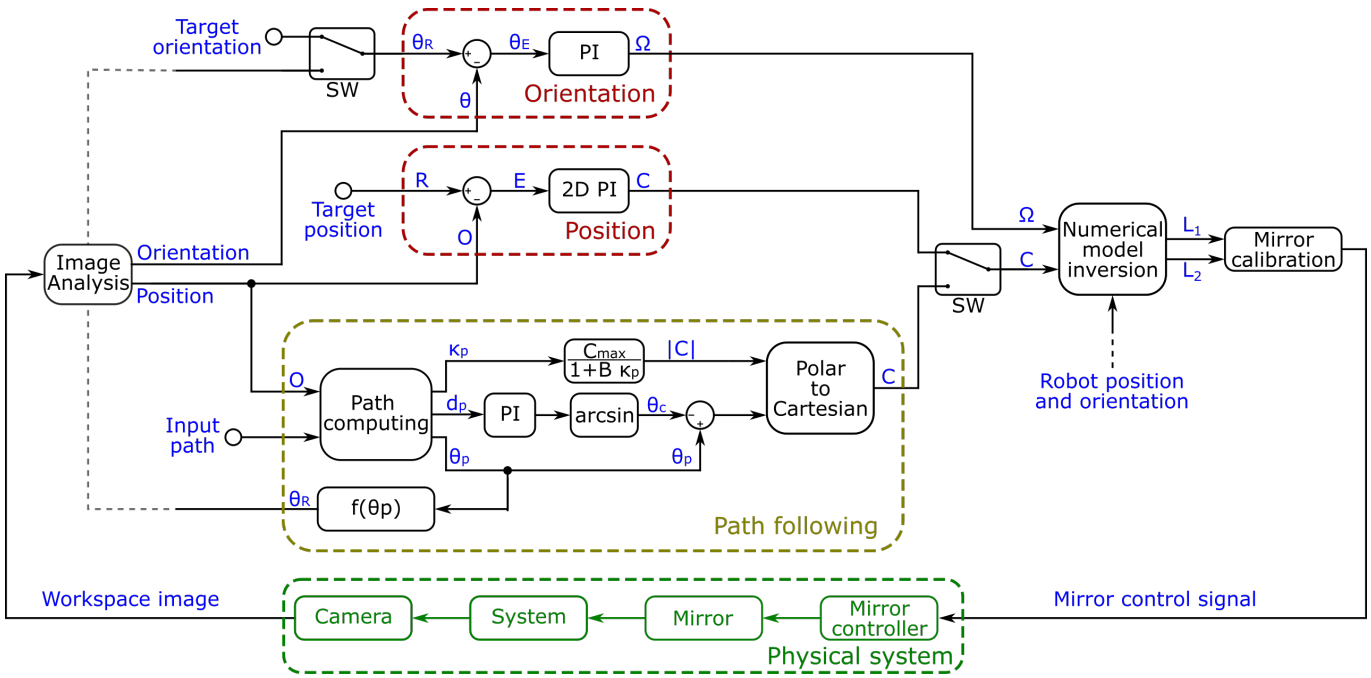

Fig. 3. Multiple-legged structure control diagram including the pose and path-following control strategies. For pose control, both switches (SW) must be up. In that case, the position and orientation control blocks (in red) compute the required actuation $\mathbf{C}$ and Ω as a function of their respective errors. For path-following control, both switches (SW) must be down. In that case, the path-following block (in yellow) computes the required actuation $\mathbf{C}$ as a function of the structure position relative to the input path, and the orientation reference θ_R as a function of the path orientation θ_p. The orientation control block, then, computes the required actuation Ω to follow θ_R. Finally, in either case, the numerical model inversion is used to compute the required laser spots positions for the computed $\mathbf{C}$ and Ω.

will likely be the one closest to the given $\mathbf{X}_0$. Since the algorithm is to be used each time step, it makes sense to use the position found in the previous time step as an initial guess, for two reasons. First, it is likely that the objective did not change that much in one time step. Second, by doing this, the algorithm will probably find the solution that is closest to the previous one, and thus minimize the distance the laser spots have to be displaced in that time step. Notice that the system (9) may not always have a solution that satisfies the physical constraints (not to shine the laser on the structure). In that case, this optimization algorithm will find the laser spot positions that produce the closest response to the commanded one. Nevertheless, most of the time a solution exists, and the system can be considered fully actuated.

Finally, this numerical model inversion can be integrated into a control loop to regulate the pose of the structure. The idea is to use standard control techniques to control the system (10), assuming $\mathbf{C}$ and Ω as inputs. Then, the previously described numerical model inversion is used to find the laser spot positions $\mathbf{L}_1$ and $\mathbf{L}_2$ that will generate these inputs.

A schema of the control loop including a pose control and a path-following with independent orientation control is shown in Fig. 3. Both control techniques are explained in the following sections.

B. Pose control

Using the numerical model inversion, we can now stabilize the position and orientation of the structure. In this case, we decompose the problem into three independent PI controllers, one for each direction and one for the orientation. To stabilize the structure position around a target $\mathbf{R}$ with a target angle θ_R, the control variables are computed as a function of the position error $\mathbf{E} = \mathbf{R} - \mathbf{O}$ and angle error $\theta_E = \theta_R - \theta$ as

$$\begin{cases} \mathbf{C} = K_{Pt}\,\mathbf{E} + K_{It}\int \mathbf{E}\,dt \\ \Omega = K_{Pr}\,\theta_E + K_{Ir}\int \theta_E\,dt. \end{cases} \tag{11}$$

With the composition of this controller and the system (10), the error dynamics in the linear regime result

$$\begin{cases} \tau_t\ddot{\mathbf{E}} + \dot{\mathbf{E}} = -\left(K_{Pt}\,\mathbf{E} + K_{It}\int \mathbf{E}\,dt\right) \\ \tau_r\ddot{\theta_E} + \dot{\theta_E} = -\left(K_{Pr}\,\theta_E + K_{Ir}\int \theta_E\,dt\right). \end{cases} \tag{12}$$

Since the systems in (12) are uncoupled and equivalent, we can write a generic error (e) dynamic equation as:

$$\frac{\partial}{\partial t}\begin{pmatrix} \dot{e} \\ e \\ \int e\,dt \end{pmatrix} = \begin{pmatrix} -\frac{1}{\tau} & -\frac{K_P}{\tau} & -\frac{K_I}{\tau} \\ 1 & 0 & 0 \\ 0 & 1 & 0 \end{pmatrix} \times \begin{pmatrix} \dot{e} \\ e \\ \int e\,dt \end{pmatrix} \tag{13}$$

By analyzing the eigenvalues of (13), we find that the system is stable if $0 < \tau K_I < K_P$.

C. Path-following

The objective of a path-following controller is to stay on the path but without any time schedule. To achieve this, the first step is to find the closest point of the path to the object

TABLE I
EXPERIMENTAL CONDITIONS.

Parameter	Value
Structure size	$10\,\mathrm{mm}$
Structure mass	$\approx 30\,\mathrm{mg}$
Water density	$997\,\mathrm{kg/m^3}$
Water viscosity	$1\,\mathrm{Pa\,s}$
Laser spot diameter	$1.3\,\mathrm{mm}$
Laser spot power	$75\,\mathrm{mW}$
Estimated α (Eq. (7))	$12\,\mathrm{mm^2/s}$
Estimated τ (Eq. (7))	$1\,\mathrm{s}$
Controllers proportional gain K_P	$0.25\,\mathrm{s^{-1}}$
Controllers integral gain K_I	$0.025\,\mathrm{s^{-2}}$

and compute the path orientation (θ_p) and curvature (κ_p) at this point. We also compute the object's coordinates in the Frenet frame on this point (tangent s_p and normal d_p). Then, if the object movement direction is θ_v, the distance to the path dynamics results [43]:

$$\dot{d_p} = \|\dot{\mathbf{O}}\| \sin\theta_e \tag{14}$$

where $\theta_e = \theta_v - \theta_p$ is the structure velocity direction relative to the path. Therefore, we define the desired advance direction as $\theta_p + \theta_C$, where θ_C is the returning angle. We propose the position control law as

$$\begin{cases} \|\mathbf{C}\| = \dfrac{C_{\max}}{1 + B\,\kappa_p} \\ \theta_C = \arcsin\left(K_{Pt}\,d_p + K_{It}\displaystyle\int d_p\,dt\right). \end{cases} \tag{15}$$

where $C_{\max}$ is the desired velocity in a straight path, B is a control parameter ($B \geq 0$), and the argument of the arcsin was saturated to $[-1, 1]$. Notably, the control velocity magnitude is reduced around high curvature sections. Using this controller and neglecting the system inertia, the distance to the path dynamic is reduced to

$$\dot{d_p} = -\|\mathbf{C}\|\left(K_{Pt}\,d_p + K_{It}\int d_p\,dt\right) \tag{16}$$

which is stable for $K_{Pt}, K_{It} > 0$.

On the other hand, for the orientation control, we define a reference orientation as a function of the path orientation ($\theta_R = f(\theta_p, t)$). As in the pose control, we define

$$\Omega = K_{Pr}\,\theta_E + K_{Ir}\int \theta_E\,dt, \tag{17}$$

where $\theta_E = \theta_R - \theta$ is the error in orientation.

IV. EXPERIMENTAL VALIDATION

The proposed control strategies have been validated experimentally in our thermocapillary manipulation platform.

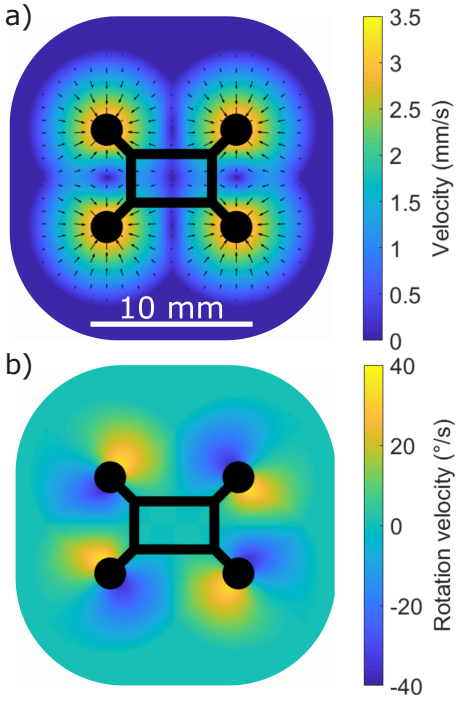

Fig. 4. Control parameters $\mathbf{C}$ (**a**) and Ω (**b**) as a function of the position of a single laser spot with a power of $75\,\mathrm{mW}$ ($\alpha \approx 12\,\mathrm{mm^2/s}$). The plots show the effect the laser spot would have if the laser spot were placed in a given position. For example, if the laser spot position is placed north of the northeast leg, the structure would move south and rotate in the negative (clockwise) direction.

A. Experimental setup

The experimental setup consists of an infrared laser pointed at a water volume from above. The laser spot is displaced by steering the laser beam with a piezoelectric tip/tilt mirror. The quick dynamics of the mirror allowed us to multiplex the laser beam into two virtual laser spots by quickly moving the laser between them. The setup is also equipped with a camera to track the objects in the workspace using standard computer vision algorithms. More details about the experimental equipment are given in the APPENDIX.

We used this platform to control a four-legged structure that stands on the interface thanks to capillary flotation [44]. For this structure and a laser spot with a power of $75\,\mathrm{mW}$, we fitted empirically the parameters of the model (7) to $\alpha \approx 12\,\mathrm{mm^2/s}$ and $\tau_t \approx \tau_r \approx 1\,\mathrm{s}$. The values of the control parameters $\mathbf{C}$ and Ω (9) as a function of the position of a single laser spot are shown in Fig. 4. In this configuration, the maximum translation and rotation velocities (keeping a minimum laser-foot distance of $1\,\mathrm{mm}$) are $4.5\,\mathrm{mm/s}$ and $40°$, respectively.

We have implemented both the pose controller and path-following controller with online model inversion in this experimental setup. The numerical model inversion takes between $1\,\mathrm{ms}$ and $5\,\mathrm{ms}$ to compute, which is compatible with our control frequency of $20\,\mathrm{Hz}$. The entire control schema is shown in Fig. 3, where the mirror calibration block computes the required mirror inputs to drive the laser to the commanded position. The experimental conditions are summarized in Table I, and the results are presented in the following sections.

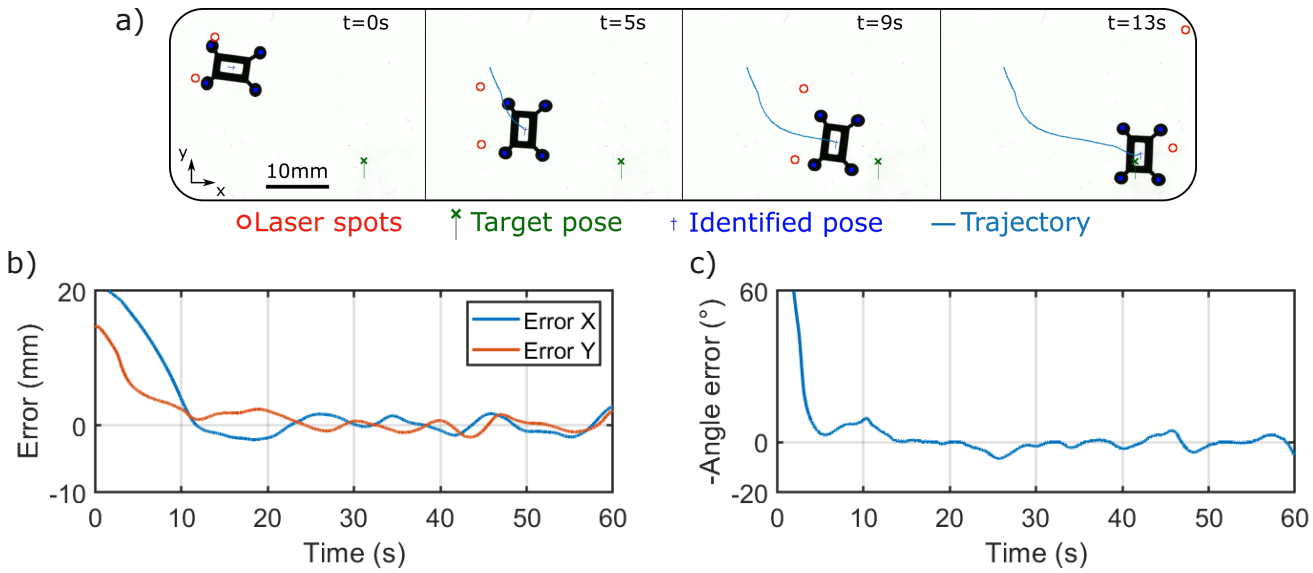

Fig. 5. Top view of the multiple-legged structure experimental pose control. The control algorithm consists in (11) with $K_{Pt} = K_{Pr} = 0.25\,\mathrm{s}^{-1}$, $K_{It} = K_{Ir} = 0.025\,\mathrm{s}^{-2}$. **a**) The trajectory of the structure. Position (**b**) and orientation (**c**) error evolution. See supplementary video.

B. Pose control results

The numerical model inversion and the pose controller described in Section III-B were implemented on the experimental setup. The gains were empirically tuned to $K_{Pt} = K_{Pr} = 0.25\,\mathrm{s}^{-1}$, $K_{It} = K_{Ir} = 0.025\,\mathrm{s}^{-2}$. An example experimental trajectory is shown in Fig. 5. Active control is still required after reaching the desired pose since the structure will slowly drift away from the target. The mean and maximum position errors (after the initial approach) are $1.5\,\mathrm{mm}$ and $3.6\,\mathrm{mm}$ ($15\,\%$ and $36\,\%$ of structure size), respectively. On the other hand, the mean and maximum angle errors are $2°$ and $7°$, respectively. This result is satisfactory, considering that the numerical model inversion algorithm found the position of the laser spots without a prescribed strategy to displace and rotate the structure. Moreover, the inversion relies on the direct model, which can differ from reality due to unmodeled phenomena (e.g., thermal inertia) or uncertainties (e.g., laser positioning errors).

C. Path-following results

The numerical model inversion and the path-following controller described in Section III-C were implemented experimentally with the same gains as the pose control case. We performed three different experiments, a constant target orientation ($\theta_R = 0$), following the path orientation ($\theta_R = \theta_p$) and the inverse of the path orientation ($\theta_R = -\theta_p$). An example of each is shown in Figs. 6 to 8 respectively.

The mean and maximum errors of the presented experiments are summarized in Table II. It can be seen that the steady-state position error in all cases is of the same order of magnitude. On the other hand, however, the orientation steady-state error is much smaller in the pose stabilization case, hinting at a link between position and orientation that was not accounted for in the model, as discussed in the following section.

TABLE II
MULTIPLE-LEGGED STRUCTURE CONTROL RESULTS SUMMARY. STEADY-STATE (AFTER INITIAL APPROACH) ERROR IN POSITION AND ORIENTATION. THESE VALUES ARE COMPUTED OVER A SINGLE PROLONGED EXPERIMENT (AT LEAST 50 s OF MOTION) EACH.

	Control case	**Pos. err.** (mm)		**Ang. err.** (°)	
		Mean	Max	Mean	Max
	Pose stabilization	1.5	3.6	1.6	6.8
Path	Constant ($\theta_R = 0$)	1.1	3.9	15.8	39.0
Path	Normal ($\theta_R = \theta_p$)	1.4	4.0	19.2	48.8
Path	Inverse ($\theta_R = -\theta_p$)	0.8	2.3	21.0	45.2

V. DISCUSSION

In this work, we have proposed a 2D pose control —-simultaneous and independent position and orientation control— based on non-contact actuation. In particular, we consider the use of laser-powered thermocapillary flows to manipulate multiple-legged structures floating at the air-water interface. First, we proposed an analytic direct model that predicts the structure response (translation and rotation) to a given laser spot position. Second, we developed a numerical model inversion tool that finds the laser spot positions that would give place to the desired response. This allows us to decouple the control of each degree of freedom (two for translation and one for rotation). Finally, a pose controller and a path-following controller were developed, utilizing the aforementioned model inversion. These controllers were then implemented and validated experimentally.

Although experimentally there could be discrepancies between the direct model and reality due to unmodeled phenomena (for example, thermal inertia) or experimental uncertainties, the closed-loop pose controller can compensate for them.

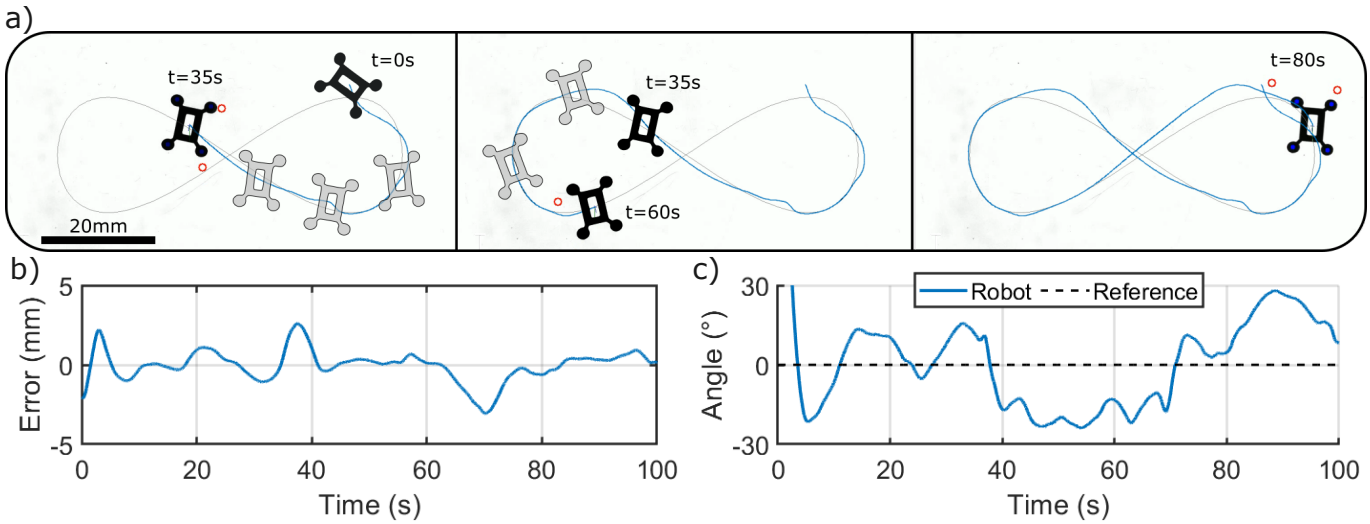

Fig. 6. Multiple-legged structure experimental path-following where the target orientation is constant. The control algorithm consists in (15) and (17) with $K_{Pt} = K_{Pr} = 0.25\,\mathrm{s}^{-1}$, $K_{It} = K_{Ir} = 0.025\,\mathrm{s}^{-2}$. **a**) The trajectory of the structure. Distance to the path (**b**) and orientation (**c**) error evolution. See supplementary video.

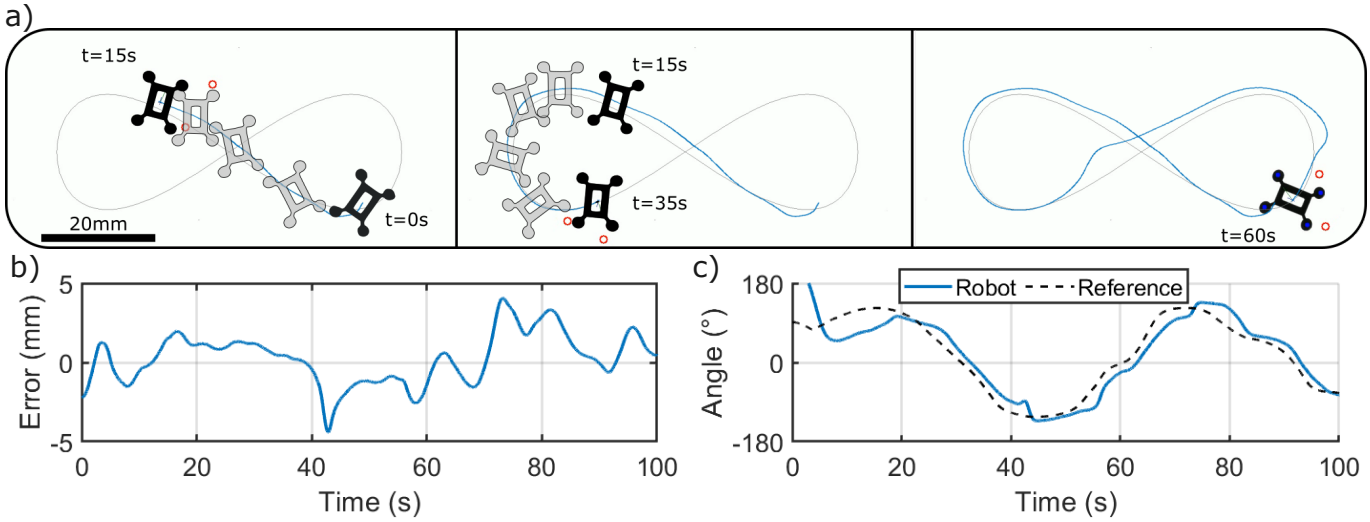

Fig. 7. Multiple-legged structure experimental path-following where the target orientation is perpendicular to the path. The control algorithm consists in (15) and (17) with $K_{Pt} = K_{Pr} = 0.25\,\mathrm{s}^{-1}$, $K_{It} = K_{Ir} = 0.025\,\mathrm{s}^{-2}$. **a**) The trajectory of the structure. Distance to the path (**b**) and orientation (**c**) error evolution. See supplementary video.

Indeed, the experimental implementation of the pose controller achieved a position and orientation precision of 0.15 body lengths and $2°$, respectively. This represents an improvement over previously reported thermocapillary actuation results [45], [46], where the precision was between 1 and 5 body lengths. For the path-following case, however, the orientation precision was much poorer, $\approx 20°$. The poorer performance in orientation control of the path-following controller can be attributed to a remaining coupling between the translation and rotation dynamics. This remaining coupling can be attributed to experimental deviations from the ideal model. Indeed, if one of the feet of the structure is immersed deeper than the rest (for example, due to fabrication errors or inhomogeneous wetting), this foot will experience a different drag force. In that case, the dynamics of the structure would be unbalanced, which would couple the translation and rotation dynamics.

Although the presented system was able to control the structure's pose, some improvements can be implemented in future studies. Concerning the hardware, one of the limitations of the current systems is the lack of online control of the laser power. Indeed, it would be advantageous to gradually decrease the laser power as the structure approaches its final position, in order for the final tuning to be done with weaker flows. Concerning the control algorithm, a possible improvement could be the integration of model-free control techniques [47], [48] to identify the system dynamics on the fly, thus increasing the system robustness to experimental uncertainties.

Finally, notice that the presented numerical inversion algorithm could be easily extended to control multiple objects, where the objective would be to find the position of up to $2N$ laser spots to control N objects. In that case, however, the complexity of the optimization algorithm grows very quickly

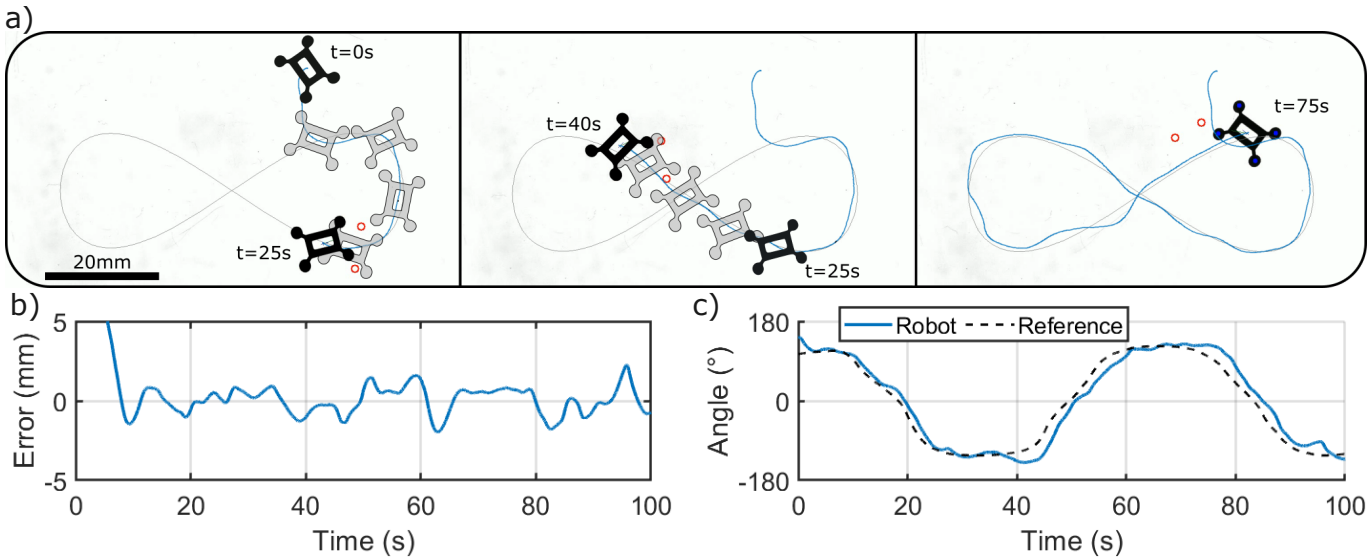

Fig. 8. Multiple-legged structure experimental path-following where the target orientation is minus the path direction. The control algorithm consists in (15) and (17) with $K_{Pt} = K_{Pr} = 0.25\,\mathrm{s}^{-1}$, $K_{It} = K_{Ir} = 0.025\,\mathrm{s}^{-2}$. **a**) The trajectory of the structure. Distance to the path (**b**) and orientation (**c**) error evolution. See supplementary video.

with the number of objects, which could be mitigated by replacing it with machine learning algorithms. On the other hand, although the presented results are on the fluid interface (thus limited to 2D), the numerical inversion approach could be easily extended to 3D systems where the position repelling or attracting points need to be defined. In conclusion, the presented results open the way towards the development of non-contact pose control of objects towards more complex micro-manipulation operations.

APPENDIX

Experimental setup. The water container is a polyethylene container filled with $8\,\mathrm{mm}$ deep layer of ultrapure water, obtained from an Arium Pro Ultrapure Water Systems. The continuous-wave laser source (Keopsys Fiber Raman Laser CRFL-01-1455-OM1-B130-FA) has a wavelength of $\lambda = 1455\,\mathrm{nm}$. The laser is guided through an optic fiber and collimated with a lens with a focal length $f = 6.24\,\mathrm{mm}$, obtaining a beam diameter of $d_L \approx 1.3\,\mathrm{mm}$ at the air-water interface. In all the considered experiments, the total laser power was $150\,\mathrm{mW}$, this is, $75\,\mathrm{mW}$ per spot. For this laser spot power, the estimated maximum thermocapillary flow velocity at the surface is around $40\,\mathrm{mm/s}$ [36], [38]. The laser beam reflects on a piezoelectric tip/tilt mirror (Mirrorcle A7M20.2-2000AL-DIP24-C/TP) and is directed to the interface. The mirror orientation is controlled by the computer through the MEMS controller, which generates the required high-voltage signals. To obtain two virtual laser spots, we profit from the quick response time of the mirror to share the laser power between two positions by switching back and forth between the two commanded positions, staying $10\,\mathrm{ms}$ on each. The multiple-legged objects were made using a Digital Light Printing setup from Kudo3D®, operated at the Laboratoire Interdisciplinaire de Physique (LIPhy). Finally, we use an IDS camera USB 3.0 UI-3370CP with a Navitar Lens NMV-75M1 to image the interface. To improve the contrast, a white backlight is placed below the water container. The frames captured by the camera are used to measure the particle position using the OpenCV 2.4.11 findContours function.

ACKNOWLEDGEMENT

This work is funded by BELSPO (IAP 7/38 MicroMAST), FNRS grant (PDR T.0129.18), and the EUR EIPHI program (Contract No. ANR-17-EURE-0002). This work has been supported by the French ROBOTEX network under Grant ANR-10- EQPX-44-01 and by the French RENATECH network and its FEMTO-ST technological facility.

REFERENCES

[1] M. Gauthier, S. Régnier, P. Rougeot, and N. Chaillet, "Analysis of forces for micromanipulations in dry and liquid media." *Journal of Micromechatronics*, vol. 3, no. 3-4, pp. 389–413, 2006.

[2] Z. Zhang, X. Wang, J. Liu, C. Dai, and Y. Sun, "Robotic micromanipulation: Fundamentals and applications," *Annual Review of Control, Robotics, and Autonomous Systems*, vol. 2, no. 1, pp. 181–203, 2019.

[3] M. A. Rahman and A. T. Ohta, "Micromanipulation with microrobots," *IEEE Open Journal of Nanotechnology*, vol. 2, pp. 8–15, 2021.

[4] E. Diller, M. Sitti *et al.*, "Micro-scale mobile robotics," *Foundations and Trends® in Robotics*, vol. 2, no. 3, pp. 143–259, 2013.

[5] F. Ongaro, S. Pane, S. Scheggi, and S. Misra, "Design of an electromagnetic setup for independent three-dimensional control of pairs of identical and nonidentical microrobots," *IEEE Transactions on Robotics*, vol. 35, no. 1, pp. 174–183, 2018.

[6] A. Barbot, H. Tan, M. Power, F. Seichepine, and G.-Z. Yang, "Floating magnetic microrobots for fiber functionalization," *Science Robotics*, vol. 4, no. 34, p. eaax8336, 2019.

[7] Z. Cenev, P. D. Harischandra, S. Nurmi, M. Latikka, V. Hynninen, R. H. Ras, J. V. Timonen, and Q. Zhou, "Ferrofluidic manipulator: Automatic manipulation of nonmagnetic microparticles at the air–ferrofluid interface," *IEEE/ASME Transactions on Mechatronics*, vol. 26, no. 4, pp. 1932–1940, 2021.

[8] Z. Wu, J. Troll, H.-H. Jeong, Q. Wei, M. Stang, F. Ziemssen, Z. Wang, M. Dong, S. Schnichels, T. Qiu *et al.*, "A swarm of slippery micropropellers penetrates the vitreous body of the eye," *Science Advances*, vol. 4, no. 11, p. eaat4388, 2018.

[9] X.-Z. Chen, J.-H. Liu, M. Dong, L. Müller, G. Chatzipirpiridis, C. Hu, A. Terzopoulou, H. Torlakcik, X. Wang, F. Mushtaq *et al.*, "Magnetically driven piezoelectric soft microswimmers for neuron-like cell delivery and neuronal differentiation," *Materials Horizons*, vol. 6, no. 7, pp. 1512–1516, 2019.
[10] M. P. Kummer, J. J. Abbott, B. E. Kratochvil, R. Borer, A. Sengul, and B. J. Nelson, "Octomag: An electromagnetic system for 5-dof wireless micromanipulation," *IEEE Transactions on Robotics*, vol. 26, no. 6, pp. 1006–1017, 2010.
[11] J. Giltinan and M. Sitti, "Simultaneous six-degree-of-freedom control of a single-body magnetic microrobot," *IEEE Robotics and Automation Letters*, vol. 4, no. 2, pp. 508–514, 2019.
[12] E. Diller, J. Giltinan, and M. Sitti, "Independent control of multiple magnetic microrobots in three dimensions," *The International Journal of Robotics Research*, vol. 32, no. 5, pp. 614–631, 2013.
[13] B. V. Johnson, S. Chowdhury, and D. J. Cappelleri, "Local magnetic field design and characterization for independent closed-loop control of multiple mobile microrobots," *IEEE/ASME Transactions on Mechatronics*, vol. 25, no. 2, pp. 526–534, 2020.
[14] H. Xie, M. Sun, X. Fan, Z. Lin, W. Chen, L. Wang, L. Dong, and Q. He, "Reconfigurable magnetic microrobot swarm: Multimode transformation, locomotion, and manipulation," *Sci. Robot*, vol. 4, no. 28, 2019.
[15] Q. Wang, D. Jin, B. Wang, N. Xia, H. Ko, B. Y. M. Ip, T. W. H. Leung, S. C. H. Yu, and L. Zhang, "Reconfigurable magnetic microswarm for accelerating tpa-mediated thrombolysis under ultrasound imaging," *IEEE/ASME Transactions on Mechatronics*, 2021.
[16] M. Baudoin and J.-L. Thomas, "Acoustic tweezers for particle and fluid micromanipulation," *Annual Review of Fluid Mechanics*, vol. 52, no. 1, 2019.
[17] Z. Ma, K. Melde, A. G. Athanassiadis, M. Schau, H. Richter, T. Qiu, and P. Fischer, "Spatial ultrasound modulation by digitally controlling microbubble arrays," *Nature Communications*, vol. 11, no. 1, pp. 1–7, 2020.
[18] A. Kopitca, K. Latifi, and Q. Zhou, "Programmable assembly of particles on a chladni plate," *Science Advances*, vol. 7, no. 39, p. eabi7716, 2021.
[19] K. Latifi, A. Kopitca, and Q. Zhou, "Model-free control for dynamic-field acoustic manipulation using reinforcement learning," *IEEE Access*, vol. 8, pp. 20 597–20 606, 2020.
[20] T. Schwarz, G. Petit-Pierre, and J. Dual, "Rotation of non-spherical micro-particles by amplitude modulation of superimposed orthogonal ultrasonic modes," *The Journal of the Acoustical Society of America*, vol. 133, no. 3, pp. 1260–1268, 2013.
[21] X. Li and C. C. Cheah, "Robotic cell manipulation using optical tweezers with unknown trapping stiffness and limited fov," *IEEE/ASME Transactions on Mechatronics*, vol. 20, no. 4, pp. 1624–1632, 2014.
[22] M. Xie, Y. Wang, G. Feng, and D. Sun, "Automated pairing manipulation of biological cells with a robot-tweezers manipulation system," *IEEE/ASME Transactions on Mechatronics*, vol. 20, no. 5, pp. 2242–2251, 2014.
[23] E. Gerena, S. Régnier, and S. Haliyo, "High-bandwidth 3-d multitrap actuation technique for 6-dof real-time control of optical robots," *IEEE Robotics and Automation Letters*, vol. 4, no. 2, pp. 647–654, 2019.
[24] Q. M. Ta and C. C. Cheah, "Multi-agent control for stochastic optical manipulation systems," *IEEE/ASME Transactions on Mechatronics*, vol. 25, no. 4, pp. 1971–1979, 2020.
[25] K. Yu, J. Yi, and J. W. Shan, "Motion control, planning and manipulation of nanowires under electric-fields in fluid suspension," *IEEE Transactions on Automation Science and Engineering*, vol. 12, no. 1, pp. 37–49, 2014.
[26] R. Pethig, "Dielectrophoresis: Status of the theory, technology, and applications," *Biomicrofluidics*, vol. 4, no. 2, p. 022811, 2010.
[27] X. Xuan, "Recent advances in direct current electrokinetic manipulation of particles for microfluidic applications," *Electrophoresis*, vol. 40, no. 18-19, pp. 2484–2513, 2019.
[28] J. Wu, X. Li, and K. Yu, "Electrophoresis-based adaptive manipulation of nanowires in fluid suspension," *IEEE/ASME Transactions on Mechatronics*, vol. 25, no. 2, pp. 638–649, 2020.
[29] A. M. Schoeler, D. N. Josephides, A. S. Chaurasia, S. Sajjadi, and P. Mesquida, "Electrophoretic manipulation of multiple-emulsion droplets," *Applied Physics Letters*, vol. 104, no. 7, p. 074104, 2014.
[30] B. Sarno, D. Heineck, M. J. Heller, and S. D. Ibsen, "Dielectrophoresis: Developments and applications from 2010 to 2020," *Electrophoresis*, vol. 42, no. 5, pp. 539–564, 2021.
[31] H. Shafiee, J. L. Caldwell, M. B. Sano, and R. V. Davalos, "Contactless dielectrophoresis: a new technique for cell manipulation," *Biomedical Microdevices*, vol. 11, no. 5, pp. 997–1006, 2009.
[32] N. Liu, Y. Lin, Y. Peng, L. Xin, T. Yue, Y. Liu, C. Ru, S. Xie, L. Dong, H. Pu *et al.*, "Automated parallel electrical characterization of cells using optically-induced dielectrophoresis," *IEEE Transactions on Automation Science and Engineering*, vol. 17, no. 2, pp. 1084–1092, 2020.
[33] A. Dalili, H. Montazerian, K. Sakthivel, N. Tasnim, and M. Hoorfar, "Dielectrophoretic manipulation of particles on a microfluidics platform with planar tilted electrodes," *Sensors and Actuators B: Chemical*, vol. 329, p. 129204, 2021.
[34] A. Lefevre, V. Gauthier, M. Gauthier, and A. Bolopion, "Closed-loop control of particles based on dielectrophoretic actuation," *IEEE/ASME Transactions on Mechatronics*, 2022.
[35] T. Michálek, A. Bolopion, Z. Hurák, and M. Gauthier, "Electrorotation of arbitrarily shaped micro-objects: modeling and experiments," *IEEE/ASME Transactions on Mechatronics*, vol. 25, no. 2, pp. 828–836, 2019.
[36] F. N. P. Basualdo, A. Bolopion, M. Gauthier, and P. Lambert, "A microrobotic platform actuated by thermocapillary flows for manipulation at the air-water interface," *Science Robotics*, vol. 6, no. 52, 2021.
[37] L. Scriven and C. Sternling, "The Marangoni effects," *Nature*, vol. 187, no. 4733, pp. 186–188, 1960.
[38] F. N. Piñan Basualdo, R. Terrazas Mallea, B. Scheid, A. Bolopion, M. Gauthier, and P. Lambert, "Effect of insoluble surfactants on a thermocapillary flow," *Physics of Fluids*, vol. 33, no. 7, 2021.
[39] A. Denasi and S. Misra, "Independent and leader–follower control for two magnetic micro-agents," *IEEE Robotics and Automation Letters*, vol. 3, no. 1, pp. 218–225, 2017.
[40] K. Levenberg, "A method for the solution of certain non-linear problems in least squares," *Quarterly of Applied Mathematics*, vol. 2, no. 2, pp. 164–168, 1944.
[41] D. W. Marquardt, "An algorithm for least-squares estimation of non-linear parameters," *Journal of the Society for Industrial and Applied Mathematics*, vol. 11, no. 2, pp. 431–441, 1963.
[42] J. J. Moré, "The levenberg-marquardt algorithm: implementation and theory," in *Numerical Analysis: Proceedings of the Biennial Conference Held at Dundee, June 28–July 1, 1977*. Springer, 2006, pp. 105–116.
[43] P. Morin and C. Samson, "Motion control of wheeled mobile robots." *Springer Handbook of Robotics*, vol. 1, pp. 799–826, 2008.
[44] D. Vella, "Floating versus sinking," *Annual Review of Fluid Mechanics*, vol. 47, pp. 115–135, 2015.
[45] R. Terrazas, A. Bolopion, J.-C. Beugnot, P. Lambert, and M. Gauthier, "Closed-loop particle motion control using laser-induced thermocapillary convective flows at the fluid/gas interface at micrometric scale," *IEEE/ASME Transactions on Mechatronics*, vol. 23, no. 4, pp. 1543–1554, 2018.
[46] R. Terrazas, D. Piron, A. Bolopion, P. Lambert, and M. Gauthier, "Thermocapillary convective flows generated by laser points or patterns: Comparison for the noncontact micromanipulation of particles at the interface," *IEEE Robotics and Automation Letters*, vol. 3, no. 4, pp. 3255–3262, 2018.
[47] M. Fliess and C. Join, "Model-free control," *International Journal of Control*, vol. 86, no. 12, pp. 2228–2252, 2013.
[48] S. Roy, J. Lee, and S. Baldi, "A new adaptive-robust design for time delay control under state-dependent stability condition," *IEEE Transactions on Control Systems Technology*, vol. 29, no. 1, pp. 420–427, 2020.

Franco Piñan Basualdo received his Ph.D. degree in Engineering Sciences and Technology at the Université Libre de Bruxelles, Belgium, and his Ph.D. degree in Automation at the Université de Bourgogne Franche-Comté, France in the framework of a double degree program in 2022. His research interests are microrobotics, automatic control, swarm robotics, microfluidics, and applied physics.

Olivier Stéphan received his Ph.D. degree in analytical chemistry in 1995 from the University of Pierre et Marie Curie, Paris, France. He is currently a teacher-researcher in physical-chemistry at the Interdisciplinary Laboratory of Physics (LiPhy), Grenoble Alpes University, France. His research interests are mainly focused on tridimensional microfabrication using laser microfabrication or Digital Light Printing.

Aude Bolopion received her Ph.D. degree in robotics in 2010 from the University of Pierre et Marie Curie, Paris, France. She is currently a CNRS researcher at the FEMTO-ST Institute, Besancon, France. She has been a member of the Biomedical Micro Nano Robotics team since 2011. Between 2007 and 2011 she was a member of the ISIR micromanipulation team. Her research interests are focused on teleoperation and haptic feedback at the nanoscale, and on noncontact micromanipulation.

Michaël Gauthier received his PhD degree in Automation and Robotics from the Université de Franche Comté, France in 2002. He is currently CNRS Senior scientific research at FEMTO-ST institute and the head of the Automation and MicroMechatronics Systems (AS2M) Department. He has been granted by the French CNRS bronze medal (Early Career Award) in 2011. His research interests are focused on microworld modeling, micro/nano manipulation, dexterous microhandling and high-speed control of non-contact micromanipulations.

Pierre Lambert received his PhD degree in engineering sciences from the Université Libre de Bruxelles, Belgium in 2004. He is currently Associate Professor at Université Libre de Bruxelles, in the field of microengineering and microfluidics. He is the coordinator of the Belgian thematic network on Microfluidics and Micromanipulation: Multiscale Applications of Surface Tension (`www.micromast.be`). His current research interests are in the fields of soft robotics (tunable stiffness mechanisms, smart catheters) and of surface tension effects in microsystems (capillary gripping, capillary self-alignment, thermocapillary micromanipulation).